Journal of Applied Meteorology, Manuscript No. **GRR–526**

Relationship between precipitation rates at the ground and aloft — a modeling study

Nikolai Dotzek and Thorsten Fehr

DLR–Institut für Physik der Atmosphäre,
Oberpfaffenhofen, D–82234 Wessling, Germany

Received 17 June 2002, in revised form 1 January 2003

Corresponding author's address:
Dr. Nikolai Dotzek
DLR–Institut für Physik der Atmosphäre,
Oberpfaffenhofen, D–82234 Wessling, Germany.
eMail: nikolai.dotzek@dlr.de, http://www.op.dlr.de/~pa4p/
Tel: +49–8153–28–1845, Fax: +49–8153–28–1841.

J. Appl. Meteor., in press.

Relationship between precipitation rates at the ground and aloft — a modeling study

Nikolai Dotzek and Thorsten Fehr

DLR–Institut für Physik der Atmosphäre,
Oberpfaffenhofen, D–82234 Wessling, Germany

Received 17 June 2002, in revised form 1 January 2003

Abstract

Two cloud–resolving mesoscale models, KAMM and MM5, were used to study reflectivity factor–rain rate relationships and instantaneous and horizontally averaged profiles of precipitation rate R for convective storms of varying intensity. Simulations were conducted for idealized terrain. KAMM modeled a single shower cloud, MM5 was used to study split storm supercell development. Both models consistently confirm analytical results from earlier studies: Convective drafts and stratification of air density significantly alter the local rain rate, and therefore also any Z–R relation relying on conditions of stagnant air and sea level air density. While air density effects can be almost completely corrected for by a recently proposed algorithm, effects of convective drafts remain. They can lead to upward precipitation mass fluxes of significant magnitude and subsequent horizontal displacement of precipitation. Applicability of simple Z–R relations over complex terrain with distinct watershed boundaries will be strongly degraded by such convection effects on precipitation mass fluxes.

Keywords: Precipitation Rate; Vertical Profile; Deep Convection; Cloud–Resolving Model

1 Introduction

As recently quantified by Dotzek and Beheng (2001) and briefly summarized here in Appendix A, standard reflectivity–to–rainfall (Z–R) relations of the form $Z = a\,R^b$ are significantly altered in deep convective clouds by convection effects on precipitation rate R, defined as vertical mass flux density of hydrometeors with diameter D and bulk density ρ_h, i. e.

$$R = \frac{\pi}{6}\rho_h \int_0^\infty n(D) D^3 w_s \, dD \quad . \tag{1}$$

Not only is R subject to variations in particle number spectra $n(D)$, but there is a much stronger dependence on the effective sedimentation velocity (Dotzek and Beheng, 2001)

$$w_s(D, w, \rho) = w + w_t(D, \rho) = w + f(\rho)\, w_{t,00}(D) \quad . \tag{2}$$

Here, w denotes ambient vertical air velocity, $w_{t,00}(D)$ is terminal fall speed of hydrometeors at sea level conditions, and effects of air density ρ are covered by $f(\rho)$. Therefore, aside from $n(D)$, variations of R may result from up and downdrafts and, secondarily, from vertical density stratification from its sea level value ρ_{00} to smaller values aloft. After integration of Eq. (1), the precipitation rate in bulk variables reads

$$R = \left[w + \bar{w}_{t,00} \left(\frac{\rho_{00}}{\rho} \right)^{\alpha} \right] \rho\, q \quad , \tag{3}$$

with $\rho\, q$ denoting hydrometeor mass per unit volume and $\bar{w}_{t,00}$ hydrometeor fall speed. The term $f(\rho)$ from Eq. (2) was chosen in its most widely used form with its best–fit value $\alpha = 0.45$ for terminal velocities after Beard (1985). Even though Beard proposed $\alpha = 0.42$ for direct rain rate computations, we have to stay with $\alpha = 0.45$, as it enters the equations from the fall speed term.

Conventionally in radar meteorology, R is taken to be positive for precipitation *falling* to the ground despite a negative $\bar{w}_s$. We will conform with that and show the negative of R defined in Eq. (3) in our graphs and Z–R and R–$\rho\, q$ relations.

Lower air density aloft increases R because hydrometeor fall speed depends on ρ in a way that lower density air exerts a smaller friction force on the falling hydrometeors, allowing them to fall faster than at sea level air density (e. g. Foote and du Toit, 1969; Battan, 1973). Dotzek et al. (2002) were able to show that, while being a secondary effect on the precipitation rate profile alone, this can have significant consequences for radar–based quantitative precipitation estimation (QPE) at large radar ranges.

Also, downdrafts increase R, while updrafts decrease the precipitation rate. In the limit of updrafts greater than the hydrometeor fall speed, R can become highly negative even for arbitrarily high hydrometeor contents by the action of strong updrafts. As noted by Dotzek and

Beheng (2001) and many other researchers before, (e. g. Battan, 1976; Aniol et al., 1980; Wilson and Brandes, 1979; Zawadzki, 1984; Austin, 1987; Joss and Waldvogel, 1990; Atlas et al., 1995; Dölling et al., 1998; Atlas et al., 1999; Jordan et al., 2000) this makes application of standard Z–R relations for deep convective clouds difficult or even questionable. Various Z–R relations, however, have been published, for instance by Battan (1973) and Sauvageot (1992).

Besides, deep moist convection also induces horizontal components and is usually superposed to strong vertically sheared mean horizontal air flow, as schematically outlined in Fig. 1. For a developing rain cell within a radar scan volume, but with no rain at the ground yet (i. e. $R_{00} = 0$), application of a Z–R relation would erroneously diagnose $R_{00} > 0$ and also a precipitation accumulation P_{ac} on the ground. In reality, rain will only reach the ground at later times and with a horizontal displacement due to combination of convection and transport by the mean wind profile. While a minor effect over large areas with homogeneous orography, this horizontal shift can become important over complex terrain with small distances between neighboring river catchments. Evidently, the rain rate for a given value of Z in convective clouds changes in space and time, and no unique Z–R relation exists in general (cf. the discussion given by Battan, 1976; Atlas et al., 1995; Dotzek and Beheng, 2001).

Practical problems of this kind in the context of QPE are usually addressed by combining data from one (cf. Dotzek et al., 2002) or several radars (cf. Gourley et al., 2002). Here, with R at the ground (where $w = 0$) being derived from Z measured by low–elevation radar scans the problem arises how to relate Z at a few kilometers above radar to an instantaneous rain rate at (or below) the radar level. Even in the case of stratiform clouds, vertical drafts, density stratification, and the profile of the horizontal wind may introduce considerable error to this non–local approach. At least, the effect of air density stratification on terminal fall velocity and, hence, on Z–R relations of the form $Z = a\ R^b$ can nearly be eliminated (Dotzek et al., 2002).

So, to supplement Dotzek and Beheng (2001) and Dotzek et al. (2002), in our paper Z–R relations and vertical profiles of instantaneous (R) and horizontally averaged ($\langle R \rangle$) precipitation rate are studied in more detail with a cloud–resolving model analysis. Despite the cloud microphysical simplifications inherent to Kessler–type bulk cloud models (Kessler, 1969), they offer the unique opportunity to compare consistent fields of hydrometeor content, vertical drafts and air density stratification. From these fields, R and Z can be computed at every grid points to conduct a study that reflects effects of deep convective motions in a stratified atmosphere alone, unbiased by microphysical processes hardly accessible for either models or observations.

The paper is organized as follows: Sec. 2 briefly presents the two model simulations applied for our study with their initialization and procedure. In Sec. 3 KAMM model results for a single cell cumulonimbus are discussed, while Sec. 4 deals with MM5 supercell and multicell storm simulations, respectively. Secs. 5 and 6 present discussion and conclusions.

2 Model setup

Two different three–dimensional nonhydrostatic mesoscale models, KAMM (Karlsruhe Atmospheric Mesoscale Model, e. g. Adrian and Fiedler, 1991; Dotzek, 1999) and MM5 (NCAR Penn State Mesoscale Model e. g. Grell et al., 1994), were used to model individual storms over idealized orography with 1 km horizontal grid size. Note that both simulations were initially conducted to clarify scientific problems other than the present one. Only after the findings by Dotzek and Beheng (2001), it appeared fruitful to exploit the two simulations to determine the influence of deep convection on vertical profiles of precipitation rate. In both case studies, model initialization was performed with a single atmospheric sounding and convection was artificially triggered by specifying local perturbations of equivalent potential temperature Θ_e (cf. Klemp and Wilhelmson, 1978).

The basic differences in both simulations are: (i) MM5 used a flat terrain while the KAMM orography had a 500 m high bell–shaped mountain in the center of the model domain, (ii) KAMM modeled a single shower cell, whereas MM5 was used for a split storm supercell simulation, and (iii) both model runs used separate initialization soundings.

2.1 KAMM

KAMM was applied in a substantially revised and extended version to simulate deep convection including a bulk microphysical cloud module predicting rain water $\rho\, q_r$, cloud water $\rho\, q_c$, and cloud ice $\rho\, q_i$ concentrations (Dotzek, 1998, 1999). Aside from the prognostic quantities $\rho\, q$ the model also provides the fields of w, ρ and terminal fall speed of hydrometeors $\bar{w}_{t,00}$. All hydrometeor fall speeds in the model are subject to a variation due to density stratification according to Eq. (3) with $\rho_{00} = 1.225$ kg m^{-3} and $\alpha = 0.45$ (Beard, 1985).

As outlined by Dotzek and Beheng (2001), for precipitation KAMM has only one prognostic quantitiy, $\rho\, q_r$. However, effects of mixed and ice–phase precipitation could be included in the KAMM model according to the simple approach by Tartaglione et al. (1996): Below freezing level height, a terminal velocity law for water drops is applied. Above the freezing level, between 0° C and -35° C, hydrometeor fall speeds follow from linear interpolation with temperature between raindrop fall speed and a constant terminal velocity $\bar{w}_{t,00} = -2.5$ m s^{-1} representative of a mixture of snow and lump graupel. For temperatures less than -35° C only this asymptotic fixed value is assumed. As Tartaglione et al. (1996) showed, storm dynamics are improved significantly by this more realistic description of hydrometeor sedimentation.

The model domain size was 64 km in both horizontal directions x and y, and 18 km in the vertical. A bell–shaped, 500 m high mountain with a half–width of 2 km was positioned in the center of the model domain. Compared to an otherwise identical simulation for flat terrain, this mountain led to an intensification of the storm as it moved over it, but for evaluation of the KAMM run in the present context this does not play a major role. Grid spacing of the model was 1 km horizontally and 10 m at ground level to about 100 m near the model top vertically. The basic state was a barotropic flow of 10 m s^{-1} from west–southwest, and the profiles of temperature and humidity were chosen similar to the synoptic setting described by Hannesen et al. (1998) in their radar analysis of a small–supercell F1 tornado in southern Germany on 9 September 1995. Profiles of virtual potential temperature Θ_v and relative humidity RH up to 10 km altitude are shown in Table 1. Note the continuous decrease of RH toward the ground below 2.5 km above ground level (AGL). With the barotropic flow in the present simulation, however, supercell formation could not be expected (Weisman and Klemp, 1982). The composite sounding from Hannesen et al. (1998) revealed a convective available potential energy (CAPE) of 440 J kg^{-1} with a level of free convection (LFC) at about 1.2 km and a neutral buoyancy level (LNB) at approximately 7.3 km AGL, allowing for overshooting cloud tops of at most 8 to 9 km AGL.

Convection was initiated by a local 3 K boundary layer Θ_e perturbation to the basic state with a moist and warm air mass centered at $(x = 10, y = 25, z = 1.5)$ km, similar to the procedure of Klemp and Wilhelmson (1978). The perturbation was introduced to the system after one hour of spin–up simulation, corresponding to 1200 local standard time (LST).

Soon after initiation a rapidly developing cumulus cloud appeared, moving east–northeastward with the mean flow. Fig. 2 shows a synthetical radar composite from the model study, a projection of maximum reflectivity values Z in the volume data to a vertical x,z plane. Reflectivity factors were computed from the prognostic bulk variables as outlined by Dotzek and

Beheng (2001) and Appendix A with identical formulas for KAMM and MM5. Light grey shading denotes reflectivities above 0 d$\mathrm{B}Z$, representative of cloud shape, dark grey areas correspond to high reflectivities of more than 40 d$\mathrm{B}Z$. The location of cloud initialization was chosen such that the storm would be in its mature stage when passing over the bell–shaped mountain in the center of the domain. At 1220 LST, Fig. 2 shows that cloud top was at about 7 km AGL (a) and a core of high reflectivity has developed. Only 10 min later, heavy precipitation fell out of the now mature cumulonimbus cloud with its top at 9 km AGL (b). The decaying stage with weakening precipitation and cloud transition to an ice–filled anvil can be seen from image (c) from 1245 LST. The highest computed reflectivities in this storm were above 60 d$\mathrm{B}Z$, initial instantaneous rain rate at the ground peaked at $420\ \mathrm{mm\,h^{-1}}$, and the largest precipitation accumulation at a single point was 34 mm. As given in Table 2, updrafts in this cloud hardly exceeded $11\ \mathrm{m\,s^{-1}}$ (at 1220 LST), downdrafts reached their peak of about $-10\ \mathrm{m\,s^{-1}}$ at 1245 LST, and a weak gust front developed at later times. However, note that gust front formation was mainly suppressed by the mountain orography: An identical simulation run over flat terrain showed a very distinct gust front with a boundary layer arc cloud moving away from the storm (Dotzek, 1999). In general, thermodynamic stratification as shown in Table 1 was responsible for enhancing precipitation–induced downdrafts. This cumulonimbus cell represents in many ways a typical Central European heavy rain shower during the warm season.

2.2 MM5

Adapted by Fehr (2000), MM5 was used for the split storm simulation over flat terrain. The Goddard Cumulus Ensemble microphysics scheme (Tao and Simpson, 1993), with cloud water $\rho\,q_c$, rain $\rho\,q_r$, cloud ice $\rho\,q_i$, snow $\rho\,q_s$ and graupel $\rho\,q_g$ as prognostic variables, was applied.

The vertical profile for model initialization was a composition of radiosonde, aircraft, and dropsonde data representative of a supercell storm situation in southern Germany on 21 July 1998. Resulting initial conditions for the case were given by Fehr (2000) and are summarized in Fig. 3 showing the model initialization sounding. Large CAPE of $1343\ \mathrm{J\,kg^{-1}}$, a convective inhibition (CIN) of $-37\ \mathrm{J\,kg^{-1}}$, and a bulk Richardson number Ri_b of 25.5 support split supercell development (Weisman and Klemp, 1984).

The simulation was run with nested grids. The coarse grid covered $363 \times 246\ \mathrm{km}^2$ with 3 km horizontal grid spacing, while the inner domain was $130 \times 130\ \mathrm{km}^2$ wide, with 1 km horizontal grid size. The high–resolution inner domain tracked the developing clouds. There were 50 vertical levels between the ground and approximately 20 km, 11 below 2 km and 12 above the tropopause. After a short spin–up time of 10 min, convection was initialized by a rather large 8 K Θ_e perturbation at 1600 LST. Smaller values for the Θ_e perturbation did not lead to a storm splitting in the early stages of cumulonimbus development, probably caused by the short spin–up time. The model was then run for 3.5 h, i. e. up to 1930 LST. At this time storm anvils reached the boundary of the inner model domain.

The complete storm development at mid–levels can be seen in Fig. 4, showing total hydrometeor mixing ratio at 4.4 km AGL and near–surface gust front location, identified by a 0.5 K drop in temperature. At 1630 LST, 30 min after convective initialization, the storm consisted of a single cell, that split into a northern left flank and a southern right flank storm during the following 30 min. The two cloud systems evolved as individual entities: The left–mover developed into a multicell (MC), the right–mover into a supercell (SC) storm (cf. Wilhelmson and Klemp, 1981; Weisman and Klemp, 1984).

As Table 2 and Fig. 4 show, storm development was supercell–dominated in the first two hours. The maximum updraft velocity remained above 30 $\mathrm{m\,s^{-1}}$ during this period, reaching values close to 50 $\mathrm{m\,s^{-1}}$ (Fehr, 2000), while maximum supercell downdraft velocities exceeded -25 $\mathrm{m\,s^{-1}}$. Storm strength (Weisman and Klemp, 1984)

$$S = \frac{w_{\max}}{\sqrt{2\,\mathrm{CAPE}}} \quad , \tag{4}$$

also given in Table 2, shows that the supercell life cycle undergoes a maximum in the middle while the multicell storm is continuously growing in strength and size. However, the vertical drafts in the multicell are generally shorter–lived than in the supercell storm. After two hours of quasi–steady state of the supercell rapidly decayed. Another example of a more vigorous left–mover development is the simulation presented by Wilhelmson and Klemp (1981).

Storm anvils reached up to 12 km AGL with a maximum overshoot of roughly 2 km, so cloud tops peaked at approximately 14 km. In its most vigorous phase, from about 60 to 120 min simulation time, strong vertical vorticity on the order of 0.01 $\mathrm{s^{-1}}$ was built up and maintained within a mesocyclone and in the boundary layer as low as 1.0 km AGL, a characteristic of supercell storms. The simultaneous development of an S–shape cloud geometry shown in the horizontal section of Fig. 4 was caused by the formation of a strong rear flank- and a weaker forward flank downdraft. This is also in accordance with the concept of supercell thunderstorms.

3 KAMM results: single cell storm

Fig. 2 shows three characteristic stages of cloud development for the single cell storm. The radar reflectivity factor computed for Fig. 2 represents the total sum of Z–values from any present hydrometeors, i. e. $Z_{\text{tot}} = Z_c + Z_i + Z_r$ (cf. Appendix A and Smith, 1984; Dotzek and Beheng, 2001).

In Fig. 2 stage (a), storm growth, a larger volume of cloud and precipitation experiences updrafts (cf. also Table 2) and reduced rain rates, than stage (b), cloud maturity, because here maximum up and downdrafts were nearly in equilibrium ($w_{\text{max}} = 5.78\,\text{m}\,\text{s}^{-1}$, $w_{\text{min}} = -5.10\,\text{m}\,\text{s}^{-1}$). In stage (c), storm decay, precipitation rates tend to be enhanced due to more dominant downdrafts.

Analyzing all three stages (a) to (c) we will first present Z–R and R–$\rho\,q$ relations with and without convective drafts. Then scatter plots giving information on individual precipitation profiles R will be shown before horizontally averaged vertical profiles of $\langle R \rangle$ provide information on mean properties of rain rates under the influence of convection.

3.1 Z–R and R–$\rho\,q$ relations

Analytical Z–R and R–$\rho\,q$ relations were given by Dotzek and Beheng (2001), focusing mainly on stage (b) in Fig. 2. From the same regression analysis, we find the following Z–R relations for KAMM's precipitation bulk hydrometeor density $\rho\,q_r$, both given without convection, and with modeled vertical drafts.

The equations give Z–R and R–$\rho\,q$ relations with their coefficients split into mean value and standard deviation as derived from a least square fit to a scatterplot from data at all model gridpoints with hydrometeors. Setting $w = 0$ in computing R from Eq. (3) assuming $\rho\,q_r$ only consists of rain water we obtain:

$$Z = [163 \pm 12]\, R^{1.54 \pm 0.01} \quad , \quad R = [23.02 \pm 1.06]\, (\rho\,q)^{1.13 \pm 0.01} \qquad \text{1220 LST,} \tag{5a}$$

$$Z = [170 \pm 26]\, R^{1.55 \pm 0.02} \quad , \quad R = [22.38 \pm 2.21]\, (\rho\,q)^{1.13 \pm 0.01} \qquad \text{1230 LST,} \tag{5b}$$

$$Z = [173 \pm 20]\, R^{1.56 \pm 0.01} \quad , \quad R = [21.63 \pm 1.61]\, (\rho\,q)^{1.12 \pm 0.01} \qquad \text{1245 LST.} \tag{5c}$$

Eqs. (5a–c) only show small scatter stemming from the density stratification of the atmosphere. Variation of mean values for prefactors and exponents of Z–R and R–$\rho\,q$ relations is not significant. Temporal variations of the standard deviation, however, can be interpreted as being influenced by the density dependence of R according to Eq. (3): Fig. 2 shows that cloud top and vertical extent of in–cloud precipitation are highest at 1230 LST, lowest at 1220 LST, and somewhere in between at 1245 LST. Accordingly, density–induced scatter also peaks at 1230 LST and is smallest at 1220 LST.

For completeness, we stress that simple inversion of the Z–R relations given in Eqs. (5a) would lead to an erroneous diagnosis of rainfall below the developing shower cloud — Fig. 2 shows that at 1220 LST all precipitation is contained within the cloud or still very close to cloud base. This is an example illustrating the schematic of Fig. 1.

The same data as before, but including the Tartaglione et al. (1996) parameterization to treat $\rho\, q_r$ as mixed–phase precipitation yields:

$$Z = [138 \pm 20]\ R^{1.59 \pm 0.03} \quad , \quad R = [20.80 \pm 1.07]\ (\rho\, q)^{1.12 \pm 0.01} \qquad \text{1220 LST,} \tag{6a}$$

$$Z = [121 \pm 40]\ R^{1.64 \pm 0.08} \quad , \quad R = [18.98 \pm 2.60]\ (\rho\, q)^{1.11 \pm 0.03} \qquad \text{1230 LST,} \tag{6b}$$

$$Z = [133 \pm 32]\ R^{1.63 \pm 0.06} \quad , \quad R = [20.37 \pm 1.21]\ (\rho\, q)^{1.12 \pm 0.02} \qquad \text{1245 LST.} \tag{6c}$$

We can expect that according to the Tartaglione et al. (1996) parameterization, cloud regions above the freezing level $\rho\, q_r$ will now represent a mixture of supercooled liquid and frozen hydrometeors. As this leads to a modification of the hydrometeor fall speeds between the extremes of rain and snow / lump graupel with constant terminal velocity, also Z–R and R–$\rho\, q$ relations should approach a form dependent on the most dominant hydrometeor form. Consequently, the exponents for Z–R relations should be between the analytical values for rain (1.54) and for snow / lump graupel (1.75), and for the R–$\rho\, q$ relation between 1.14 and 1.00, respectively (cf. Appendix A and Dotzek and Beheng, 2001). Eqs. (6a–c) indeed show such a tendency, again strongest for 1230 LST when cloud top is highest. Simultaneously, mean values of Z–R prefactors decrease, while their standard deviation slightly increases.

Finally including mixed–phase precipitation and convection, $w \neq 0$ in Eq. (3) leads to:

$$Z = [715 \pm 495]\ R^{1.75 \pm 0.24} \quad , \quad R = [\ 7.36 \pm 3.36]\ (\rho\, q)^{0.89 \pm 0.12} \qquad \text{1220 LST,} \tag{7a}$$

$$Z = [197 \pm \ 94]\ R^{1.55 \pm 0.11} \quad , \quad R = [18.55 \pm 7.29]\ (\rho\, q)^{1.12 \pm 0.10} \qquad \text{1230 LST,} \tag{7b}$$

$$Z = [112 \pm \ 49]\ R^{1.55 \pm 0.10} \quad , \quad R = [28.17 \pm 5.80]\ (\rho\, q)^{1.17 \pm 0.05} \qquad \text{1245 LST.} \tag{7c}$$

Influences from density stratification or mixed–phase hydrometeor ensembles are indeed minor compared to the effect of vertical convective drafts, as obvious from Eqs. (7a–c). Now, just by including the modeled vertical drafts, large scatter occurrs. Also the mean values of prefactors and exponents undergo significant changes. As already found by Dotzek and Beheng (2001) for the data from 1230 LST, our present evaluation of all three cloud stages substantiates the dominant influence of convection on Z–R relations even more. Storm maturity at 1230 LST is closest to the relations with $w = 0$. Up- and downdrafts, as well as their variances, have similar magnitudes there. We focus here on the two other times, as they show the most drastic changes in their average Z–R and R–$\rho\, q$ relations.

At 1220 LST updrafts are strongest, cloud top is well above the freezing level (at about 3.0 km AGL) and the high precipitation content only begins to fall out from cloud base, cf. Fig. 2. We can expect that precipitation rates are strongly reduced due to the updrafts, most prominent during cloud growth. As soon as precipitation–cooled downdrafts dominate cloud dynamics, rain rates should be enhanced. Eq. (7a) shows very strong variation in the prefactors of both Z–R and R–$\rho\, q$ relations. For the latter, the prefactor is reduced by almost 65 % and the exponent's variation encompasses 1.00 — the value appropriate for hydrometeors falling at constant terminal velocity. The fact that the mean value of the exponent is below 0.9 may be attributed to the way mixed–phase precipitation is represented by the Tartaglione et al. (1996) parameterization. Similarly, the Z–R prefactor attains a very high value consistent with observed Z–R relations reported for thunderstorms, and the exponent of about 1.75 again points at particles falling at constant speed (cf. Dotzek and Beheng, 2001).

The reason for this behavior cannot be a larger proportion of ice phase precipitation, as comparison with Eq. (6a) reveals. The amount of hydrometeors in the ice phase is the same in both cases. Instead, a probable explanation is that during storm growth a large amount of water phase precipitation falls at constant speed, namely the speed $w_s \simeq 0$. This accumulation of hydrometeors floating at constant altitude in the updraft leads to the observed exponents and prefactors.

At 1245 LST on the other hand, updrafts no longer play a relevant role in the decaying cloud and its rain shaft. As Eq. (7c) shows, both Z–R and R–$\rho\, q$ relations do show enhanced rain rates but prefactors and exponents are relatively close to their values from Eq. (6c) and their analytical ranges. Again, the mean value of the R–$\rho\, q$ exponent slightly exceeds its analytical bound of 1.14. Table 2 gives a maximum downdraft speed of –9.75 $\mathrm{m\,s^{-1}}$ which can roughly double typical terminal velocities in heavy rain.

3.2 Individual rain rate profiles

Information on individual horizontal grid point vertical profiles $R(z)$ and the total vertical mass flux budget $R_{\rm tot} = R_c + R_i + R_r$ can be gathered from the scatter plots of R and z shown in Fig. 5a–f for the modeled cumulonimbus cloud of Fig. 2. For all grid points within the cloud and the rain shaft, $R(x, y, z) = R(\boldsymbol{r}, z)$ was evaluated from Eq. (3) using w, ρ and the hydrometeor concentrations $\rho\, q$. Individual hydrometeor types are distinguished by symbols for precipitation (rain or snow / lump graupel, $+$), cloud ice ($*$), and cloud water ($\circ$), respectively. Whenever $R_{\rm tot}$ exceeds the contribution of any single hydrometeor type, it is plotted by a cross ($\times$).

Figs. 5a,c,e exclude vertical air motions, thereby providing the traditional view of precipitation falling through stagnant air. Figs. 5b,d,f include vertical air motions, and give the real hydrometeor mass flux profiles.

At 1220 LST the scatter plot in Fig. 5a gives a triangular shape of the hydrometeor mass flux distribution. Note the similarity between our Fig. 5a and the rain rate profiles presented in the analytical study by Wacker and Seifert (2001). Clearly, at this point in time we observe sedimentation of primary precipitation inside the cloud, there is no secondary rain formation going on yet. Hardly any symbols other than those for precipitation or the total rain rate can be seen, i. e. mass fluxes of cloud ice and cloud water are negligible for $w = 0$. This changes when $w \neq 0$ is taken into account. In Fig. 5b, a completely different view is presented: Updraft speeds in the cumulonimbus cloud at stage (a) in Fig. 2 were large, so some portions of the hydrometeors were no longer descending to the ground but rising upward. These give rise to negative precipitation rates R. Even slowly subsiding hydrometeors like cloud ice and, more so, cloud droplets can yield high upward mass fluxes exceeding 100 mm h^{-1} due to strong updrafts.

Most obvious from Figs. 5c–f is a distinct spatial coherence of the downdrafts enhancing R. The data points reveal several discrete profiles corresponding to those model grid columns containing the main downdraft. While Figs. 5c,e show development towards vertically homogeneous rain rate profiles below the freezing level at about 3 km AGL, the corresponding Figs. 5d,f reveal negative mass fluxes above 5 km AGL and strongly enhanced precipitation rates below 4 km AGL in Fig. 5d. While the largest instantaneous rain rate at the ground for this modeled cumulonimbus was 420 mm h^{-1}, the absolute maximum is $R \simeq 675$ mm h^{-1} at $z \simeq 900$ m. In Fig. 5f the largest precipitation rate is located at the 3 km AGL level, and the remnants of weak updrafts in the anvil region above 6.5 km altitude can only induce small negative mass fluxes.

3.3 Horizontally averaged rain rate profiles

Turning towards horizontally averaged precipitation rate profiles, at each vertical grid column in the model, R_{tot} was averaged over 500 m vertical intervals provided the total hydrometeor content at grid points was larger than $10^{-3}\ \mathrm{g\,m^{-3}}$. The resulting vertical profiles with 500 m spatial resolution were horizontally averaged to yield $\langle R \rangle$.

Fig. 6a gives the profiles without convective drafts. Again, for 1220 LST a triangular shape of $\langle R \rangle$ indicative of pure sedimentation is obvious (cf. Wacker and Seifert, 2001), while precipitation near the ground peaks only later at 1230 LST. Fig. 6b with convection identifies those regions where even in horizontal averages considerable upward hydrometeor mass flux occurs and also the downdraft–induced shift of maximum rain rate at 1245 LST near 1 km AGL.

Note the sharp drop in precipitation rate at about 1.75 km AGL which is evident from both Figs. 6a,b. The reason for this phenomenon not visible in the individual profiles of Figs. 5 could be identified by careful inspection of the KAMM data. It is not caused by updrafts or diminished downdrafts between 1.5 km and 2.25 km AGL — this would be visible in the individual grid point data of Figs. 5 as well. Instead it is caused by a larger horizontal extent of the cloud droplet region at this level close to cloud base: The shower cloud itself is quite small in horizontal extent. When there is lateral cloud growth near cloud base, the relative change in horizontal cloud section area is large, while the total hydrometeor mass flux over this area on the other hand remains nearly unaltered. So the observed drop in $\langle R \rangle$ is a purely geometrical averaging effect.

This explanation is substantiated by Fig. 6c giving the mass flux profiles for cloud water only. We see that at 1230 and 1245 LST the average cloud water mass flux is zero. Correspondingly, Fig. 6d depicts the mass flux of solely cloud ice and precipitation. Compared to Fig. 6b, there is no drop in rain rate any more.

A physical interpretation of this effect is readily at hand. During their lifetime, liquid precipitation particles evaporate as soon as the local relative humidity is less than 100 %. KAMM's bulk microphysical scheme includes this effect. As mentioned earlier, the thermodynamic stratification chosen for this model run supported relatively strong evaporation below cloud base: The decrease in relative humidity towards the ground below 2.5 km AGL visible in Table 1 is evidence for strong downdraft potential. An identical simulation for flat terrain led to gust front formation driven by evaporatively cooled downdrafts. So in this case, rain falling through cloud base has led to a shallow layer with condensation of cloud droplets which can explain the lateral cloud growth near cloud base.

4 MM5 results: initial cell, supercell, and multicell storms

Similar to snapshots taken from the KAMM simulation shown in Fig. 2a–c, the chosen MM5 volume data sets comprise the initial cloud stage before storm splitting ($t = 30$ min, 1630 LST), cloud maturity after splitting ($t = 90$ min, 1730 LST), and storm decay ($t = 210$ min, 1930 LST) for both the multicell and supercell storms. This is illustrated by Fig. 4, providing a plan view of total hydrometeor fields at 4.4 km AGL and gust front location during 3 h of simulated storm development. Our analysis will follow the same lines as for the KAMM evaluation. In special, the formulas to determine Z from the modeled hydrometeor fields $\rho\, q$ were identical to those used with the KAMM model, in order not to introduce any bias which might complicate comparison of the two simulations.

4.1 Initial cell (IC)

Focusing first on the initial single cell MM5 storm there is one big difference from the KAMM storm in its stage (a) from Fig. 2 aside from the larger storm strength S (cf. Table 2): This initial cell is already strongly precipitating with a rain rate at the ground of about 300 mm h^{-1}.

Looking first at Z–R and R–$\rho\, q$ relations of the initial cell without convection, relations very similar to that for the KAMM model occur:

$$Z = [169 \pm \ 10]\, R^{1.55 \pm 0.01}\,, \quad R = [22.26 \pm 0.81]\, (\rho\, q)^{1.13 \pm 0.004} \qquad \text{1630 LST.} \qquad (8)$$

This was to be expected because for stagnant air these relations are fully determined by the cloud microphysical parameterizations chosen in the particular model under consideration. Due to the principal similarity of KAMM and MM5 as bulk cloud models, the relations for air at rest must also be similar.

If convection is allowed for, then the following relations appear:

$$Z = [264 \pm 119]\, R^{1.41 \pm 0.11}\,, \quad R = [23.95 \pm 7.70]\, (\rho\, q)^{1.20 \pm 0.08} \qquad \text{1630 LST.} \qquad (9)$$

Large scatter occurrs which encompasses again well–known separate prefactors for rain and thunderstorm cloud bursts.

The scatter plot of Fig. 7a,b reveals drastic changes from the vertical distribution of rain rate depending on if w is set to zero or not. There is a slight similarity between KAMM's Fig 5c and Fig. 7a concerning the shape of the distribution. The effects of vertical drafts in Fig. 7b, however, are much more prominent in this larger storm cell than for the rain shower modeled by KAMM.

A large maximum in precipitation rate is found at about 500 m AGL due to the rain–induced downdrafts, nearly two times the value of 300 $\mathrm{mm\,h^{-1}}$ at the ground. Above 2 km AGL the mass flux becomes strongly negative, with R_{tot} ($\times$) peaking at nearly -500 $\mathrm{mm\,h^{-1}}$ at 5.5 km altitude. This total mass flux consists of several contributions, rain and graupel ($+$) peaking at –300 $\mathrm{mm\,h^{-1}}$ at 6 km AGL, cloud ice and snow ($*$) peaking at –100 $\mathrm{mm\,h^{-1}}$ at 10 km AGL, and cloud water peaking at –200 $\mathrm{mm\,h^{-1}}$ at 2 km AGL.

4.2 Supercell (SC)

Without convection, radar meteorological relations are again mainly determined by model parameterizations. Only the density effect plays a minor role:

$$Z = [170 \pm 10]\, R^{1.54\pm0.01} \quad , \quad R = [22.37 \pm 0.84]\, (\rho\, q)^{1.13\pm0.004} \qquad \text{1730 LST,} \qquad (10a)$$

$$Z = [170 \pm \;\, 9]\, R^{1.55\pm0.01} \quad , \quad R = [22.29 \pm 0.78]\, (\rho\, q)^{1.13\pm0.01} \qquad \text{1930 LST.} \qquad (10b)$$

With convection, the relations are of course affected, yet with little time dependence:

$$Z = [158 \pm 38]\, R^{1.47\pm0.05} \quad , \quad R = [26.23 \pm 4.20]\, (\rho\, q)^{1.16\pm0.03} \qquad \text{1730 LST,} \qquad (11a)$$

$$Z = [157 \pm 35]\, R^{1.46\pm0.06} \quad , \quad R = [26.02 \pm 3.88]\, (\rho\, q)^{1.17\pm0.04} \qquad \text{1930 LST.} \qquad (11b)$$

Even though at 1730 LST and 1930 LST the supercell is in very different stages of development, Z–R and R–$\rho\, q$ relations do not reflect variations in cloud evolution in any significant way. This corresponds nicely to the notion that supercells should indeed be in a quasi–stationary dynamical mode up to their decay.

This homogeneity is not so obvious from the scatter plots in Figs. 8a–d. At 1730 LST we see from panel (a) a strong increase in precipitation near and below the freezing level at 3.9 km AGL. This freezing level altitude is valid for the reference environmental sounding from Fig. 3, but not necessarily so for in–cloud regions where lifting of warm boundary layer air is likely to deform the $T = 0^\circ$ C plane and to raise it by a few hundred meters. Above and below

$T = 0^\circ$ C, rain rates are relatively homogeneous with height — indicating that the warm rain parameterization in MM5 is simply switched off above the freezing level. This is a subject inviting future investigation.

Fig. 8b shows the largest values of total precipitation rate including convection for all MM5 data under consideration. Total mass flux peaks at 650 mm h^{-1} at $z = 1.3$ km and -750 mm h^{-1} at 8 km AGL. Individual upward contributions to total mass flux at this level mainly stem from graupel ($+$) and snow ($*$).

Figs. 8c,d for 1930 LST give similarly shaped distributions, yet with much smaller values for the mass flux. Without convection there is still a small discontinuity in rainfall intensity at 4.0 km AGL. For the case $w \neq 0$ both peak levels of rain rate have moved downward coupled to the sedimentation of precipitation cores during storm decay.

Horizontally averaged precipitation rate profiles $\langle R\rangle(z)$ in Figs. 9a,b yield much smaller values than those from KAMM in Fig. 6. This is not surprising: The longer–lived and larger storms from the MM5 simulation have well–developed "passive" cloud regions with low precipitation around the main rain shafts, whereas the small and short–lived KAMM shower cell had practically no weak intensity fringes in its active life stages. Furthermore, it should be kept in mind that the two initialization soundings were significantly different. Fig. 9a gives a rather smooth decrease of $\langle R\rangle$ with height. Fig. 9b, on the other hand, gives negative mean rain rates above 3.9 km for the inital cell at 1630 LST and the supercell at 1730 LST. During storm decay at 1930 LST average mass flux is negligible above 3.9 km, the freezing level.

All profiles intersect at $\langle R\rangle = 0$ in the freezing layer region. Below that the increase towards the ground is nearly linear for all three storm stages chosen.

4.3 Multicell (MC)

Switching off convection in the analysis of the multicell storm again yields the by now already familiar Z–R and R–$\rho\, q$ relations:

$$Z = [171 \pm 10]\, R^{1.54\pm0.01} \quad , \quad R = [22.29 \pm 0.86]\, (\rho\, q)^{1.13\pm0.01} \qquad \text{1730 LST,} \quad (12a)$$

$$Z = [169 \pm 10]\, R^{1.54\pm0.01} \quad , \quad R = [22.36 \pm 0.82]\, (\rho\, q)^{1.13\pm0.004} \qquad \text{1930 LST.} \quad (12b)$$

With convection, the resulting changes are discernible but not as large as for the supercell's most active stage or even the KAMM cell:

$$Z = [172 \pm 51]\, R^{1.46\pm0.07} \quad , \quad R = [25.66 \pm 5.17]\, (\rho\, q)^{1.17\pm0.05} \qquad \text{1730 LST,} \quad (13a)$$

$$Z = [181 \pm 54]\, R^{1.49\pm0.07} \quad , \quad R = [22.37 \pm 4.38]\, (\rho\, q)^{1.13\pm0.05} \qquad \text{1930 LST.} \quad (13b)$$

It is likely that this is due to the fact that, by defiition, in multicells there is always a mixture of individual precipitation cores at different stages of evolution. Treating them all as a single large entity surely leads to some sort of intrinsic averaging. Therefore we find prefactors in the Z–R and R–$\rho\, q$ relations with mean values close to normal, i. e. the case of stagnant air, but with a higher standard deviation as for the supercell storm.

Figs. 10a–d indeed show that the shape of the scatter plots for the multicell storm is quite invariant of cloud evolution. Without convection, the jump in mass flux below the freezing level again becomes apparent from Figs. 10a,c. Below 3.9 km AGL precipitation rates are constant with height at about 190 $\text{mm}\,\text{h}^{-1}$. With convection, the S–shape of the distribution is characterized by a maximum rain rate of 450 to 480 $\text{mm}\,\text{h}^{-1}$ at 1.6 km AGL and a minimum of -520 to -420 $\text{mm}\,\text{h}^{-1}$ at 7.5 to 8.5 km AGL. From the higher density of symbols in Fig. 10d compared to Fig. 10b (as well as from Fig. 4) we can infer that the multicell storm complex has continuously grown in size and also lightly intensified during its life cycle. That left–movers need not decay quickly in principle was already shown by Wilhelmson and Klemp (1981).

Horizontally averaged precipitation profiles in Figs. 11a,b reveal the vital dynamical difference between the initial single cell at 1630 LST and the left–moving multicell. The latter leads to profiles similar to each other, both with and without convection. Again, all three mean profiles intersect around the freezing level when $w \neq 0$. The biggest difference between multicell and supercell with $w \neq 0$ as given in Fig. 9b is that for the multicell the shape of the $\langle R\rangle(z)$ profiles above the freezing level is preserved over time, however, with smaller amplitude. This was not the case for the supercell.

5 Discussion

In our modeling study we have compared the influence of convective drafts on vertical profiles of precipitation rate for the whole spectrum of storm intensities, ranging from a shower cell to a mature supercell thunderstorm. For both KAMM and MM5, Z–R relations and $R(\boldsymbol{r}, z)$ scatterplots for individual grid points, as well as horizontally averaged $\langle R\rangle(z)$ profiles consistently show the limitations of the nonlocal approach to derive R at the ground from Z aloft.

If convective drafts were set to zero, resembling the case of purely stratiform rainclouds, Z–R relations showed limited scatter due to increasing rain rate caused by air density decreasing with height. This effect on Z–R relations, however, can completely be compensated by the correction term for measured reflectivity as given by Dotzek and Beheng (2001). Application of this physically based Z–correction to observational radar network data from a stratiform rain event in central Oklahoma (Dotzek et al., 2002) showed an increase in precipitation accumulation of 10 to 50 % at radar ranges from 100 to 300 km, at which even the base–level 0.5° tilt angle radar beam is at several kilometers altitude. Note that the correction term given here by Eq. (26) in Appendix A also applies for convective clouds of any intensity. Therefore after removal of artifacts in radar–observed reflectivity fields, like the melting layer signature, it should be routinely applied to any radar observation intended to serve for quantitative precipitation estimation.

Nevertheless, for horizontally averaged vertical profiles of rain rate, both KAMM and MM5 showed that in general the correlation of precipitation mass flux aloft with rain intensity at the ground decreases rapidly over the lowest kilometers above ground — in accordance with the observed radar reflectivity correlation profile presented by Dotzek et al. (2002).

Including vertical air motion, however, very large scatter occurs in the Z–R relation at individual locations in convective clouds and in the rain–filled downdraft. Precipitation rate R is easily increased by a factor of 2 in these regions. Maximum values of rain rate consistently occur for both mesoscale models at a height of roughly 1 km AGL. Here, the precipitation–driven downdrafts reach their largest magnitude, while at lower levels increasing interaction of the downward–moving air with the ground leads to a locally high dynamic perturbation pressure under the rain shaft, decelerating the downward airflow.

The horizontally averaged $\langle R\rangle(z)$ profiles from the KAMM model attain large negative values of more than -20 mm h^{-1} in upper cloud regions during cloud growth and maturity. As the KAMM cloud is a single and short–lived shower cell, there is not much time to develop a significant "passive", low–reflectivity fringe around the core of the storm. Instead, the cloud is almost in its whole volume also precipitation–filled. Besides higher instantaneous rain rates in the MM5 simulation, this leads to the larger magnitude of the averaged KAMM rain rates compared to the MM5 storms — and also to the significant drop in average precipitation rate as soon as the cloud droplet region grows in size near cloud base.

Our MM5 results for large and strong cumulonimbus clouds confirm the KAMM data. One has to keep in mind, though, that for the more intense thunderstorms from the MM5 study a completely different sounding was used for initialization. In addition, the MM5 storms develop considerably larger regions with low Z–values around their main precipitation cores during their longer life–cycles. This leads to the somewhat smaller magnitude of the horizontally averaged $\langle R\rangle(z)$ profiles. Nevertheless, these also become negative and reach their minimum values of -18 mm h^{-1} at 5.5 km altitude.

In the split storm MM5 simulation, there is a fundamental difference between the right- and left–moving storms. The supercell showed quite stationary Z–R relations at 1730 and 1930 LST, but more time–dependent $R(\boldsymbol{r}, z)$–z scatterplots at these times. The contrary was true for the left–moving multicell storms. Here, Z–R relations showed stronger time dependence than the $R(\boldsymbol{r}, z)$–z scatterplots. A reason for this might be that the supercell, being quasi–stationary dynamically, always maintains very similar convection–influenced Z–R relations throughout its whole lifecycle. The scatterplots, however, better represent the development of the storm from maturity to decay from 1730 to 1930 LST, leading to smaller magnitudes of rain rate while still following the average Z–R relation.

The multicell, on the other hand, almost always contains a similar spectrum of cell intensities, therefore inducing more or less stationary R–z scatterplots. But the Z–R relation is more affected by the actual number of gridpoints contained within cells of a particular intensity. Thus, we observe a larger variation here.

We did not analyze in detail the horizontal transport of hydrometeors as a consequence of upward in–cloud mass fluxes as schematically outlined in Fig. 1. This would be a more fruitful task for thunderstorm simulations over highly–resolved complex terrain. However, for the growing shower cloud at 1220 LST the KAMM model was able to reproduce the sedimentation–dominated rain rate profiles described by Wacker and Seifert (2001) in their analytical study. Both in the $R(\boldsymbol{r}, z)$–z scatterplot and the $\langle R\rangle(z)$ profile, the typical triangular shape of the profile became evident.

6 Conclusions

From our modeling study the following conclusions can be drawn:

- Individual vertical profiles of R can attain large negative values in the presence of strong updrafts. The same also holds for horizontally averaged profiles of $\langle R \rangle$,
- Rapid decorrelation of $\langle R \rangle(z)$ from R_{00} significantly limits the applicability of Z aloft to determine R at the ground,
- Using Z–R relations merely in sub–regions of convective clouds will most likely not yield meaningful results,
- Maximum rain rate enhancement due to downdrafts occurs at about 1 km AGL. Below this level, vertical perturbation pressure gradient forces decelerate the downdrafts,
- Temporal variability of Z–R relations, and instantaneous rain rates versus height, were significantly different for the supercell and the multicell storms,
- In QPE, radar–observed Z–values should be corrected to eliminate the influence of air density profile on R by the physical correction procedure outlined by Dotzek and Beheng (2001) and tested using radar data by Dotzek et al. (2002),
- The same is true for model–derived precipitation, should it be computed from reflectivity instead of directly computing R from cloud microphysical model variables.

Over complex terrain, horizontal displacement of precipitation plays an additional critical role.

Acknowledgments

The authors would like to tank J. J. Gourley at NOAA–NSSL for many stimulating talks. Insightful comments by our referees greatly helped to finalize the paper. This work was partly funded by the Commission of the European Communities under contract ENV4–CT97–0409, and by the German Ministry for Education and Research BMBF under contract 07ATF 45 in the project VERTIKATOR (*Vertikaler Austausch und Orographie*, vertical transport and orography) within the atmospheric research program AFO 2000.

A Derivation of Z–R relations

In this section we give a brief outline of the analytical procedure described by Dotzek and Beheng (2001). Normalized Γ–type number distribution functions are assumed for any hydrometeor type:

$$n(D) = N_0 \, \frac{\Gamma(4)}{\Gamma(\gamma+3)} \, \left(\frac{D}{D_0}\right)^{\gamma-1} \, e^{-D/D_0} \quad . \tag{14}$$

Here D denotes particle diameter and γ is a shape parameter. N_0 presents a "particle load" of the distribution, and D_0 is a formal scaling diameter (in fact, $D_0 \equiv 1/\lambda$ in the notation of Marshall and Palmer, 1948) which can easily be related to any specific measure of particle size, such as the volume median diameter.

The normalization in Eq. (14) assures that hydrometeor content $\rho\, q$ does not depend on the shape parameter γ, cf. Eq. (16), and that for $\gamma = 1$ the exponential Marshall and Palmer (1948) spectrum is reproduced. With increasing γ the spectra broaden and conserve $\rho\, q$ by lowering $n_{\max}$. We define the moment M_m of order m by

$$M_m = \int\limits_0^\infty n(D) D^m \, dD = \frac{\Gamma(4)}{\Gamma(\gamma+3)} \, \Gamma(\gamma+m) \, N_0 \, {D_0}^{m+1} \quad . \tag{15}$$

Most bulk microphysics cloud models following the work of Kessler (1969) use hydrometeor content $\rho\, q$ as the main prognostic variable:

$$\rho\, q = \frac{\pi}{6} \rho_h \, M_3 = \pi \rho_h N_0 \, {D_0}^4 \quad . \tag{16}$$

Spectral parameters can be substituted by the moments M, so the quantity $\rho\, q$ from Eq. (16) will be introduced to any following equation to eliminate either N_0 or D_0, depending on which spectral parameter aside from $\rho\, q$ is chosen to describe the particle spectrum. Note that this does not imply any loss of generality for the spectra. Neither N_0, D_0, γ nor $\rho\, q$ are assumed as constant, and all these quantities can be functions of time and space.

A.1 Radar reflectivity factor

The radar reflectivity factor Z for spherical particles under the assumption of Rayleigh's approximation (radar wavelength much larger than particle size) is given by

$$Z = M_6 = \Gamma(4) \, \frac{\Gamma(\gamma+6)}{\Gamma(\gamma+3)} \, N_0 \, {D_0}^7 = \Gamma(4) \, (\gamma+5)(\gamma+4)(\gamma+3) \, N_0 \, {D_0}^7 \quad . \tag{17}$$

From Eq. (16) we arrive at the following two desired relationships between Z and $\rho\, q$ by eliminating either D_0 or N_0:

$$Z = \frac{\Gamma(4)}{[\pi \rho_h]^{7/4}} \,(\gamma+5)(\gamma+4)(\gamma+3)\; {N_0}^{-3/4}\, (\rho\, q)^{7/4} \tag{18a}$$

$$Z = \frac{\Gamma(4)}{\pi \rho_h} \quad (\gamma+5)(\gamma+4)(\gamma+3)\; {D_0}^{3} \qquad \rho\, q \quad . \tag{18b}$$

Note that the Z–R relation of Eq. (18b) being linear in $\rho\, q$ is related to equilibrium or statistically stationary rain (cf. Jameson and Kostinski, 2002, and references therein). However, most published Z–$\rho\, q$ relations show the power $7/4$ (Kessler, 1969) or similar empirical values like 1.82 (Douglas, 1964; Smith et al., 1975) for rain. Clearly, Z does not depend on either vertical velocity or on the variation of fall speed due to the vertical air density gradient.

A.2 Terminal fall velocity and precipitation rate

Specifying the index "00" for all quantities at the chosen reference level, i. e. sea level conditions with vertical air velocity $w = 0$, air density $\rho = \rho_{00}$, first the terminal fall velocity $w_{t,00}$ of the hydrometeors as a function of $\rho\, q$ will be computed by setting

$$w_{t,00}(D) = w_0 \, \left(\frac{D}{\hat{D}}\right)^{\beta} \quad . \tag{19}$$

Here $\hat{D}$ is the unit diameter, usually 1 mm and w_0 is the terminal fall velocity of hydrometeors with $D \equiv \hat{D}$. For rain, Kessler (1969) proposed $w_0 = -4.11 \text{ m s}^{-1}$ and $\beta = 1/2$. Using Eq. (19) a volume–weighted mean fall velocity $\bar{w}_{t,00}$ can be calculated:

$$\bar{w}_{t,00} = \frac{\pi \rho_h}{6 \rho\, q} \int_0^\infty n(D)\; w_{t,00}(D)\; D^3 \; dD \tag{20}$$

which is, after multiplication by $\rho\, q$, identical to the mean mass flux density or precipitation rate R. In Eq. (20) again either N_0 or D_0 can be eliminated introducing the hydrometeor content from Eq. (16):

$$\bar{w}_{t,00} = \frac{w_0}{[\pi \rho_h]^{\beta/4}} \, \frac{\Gamma(\gamma+3+\beta)}{\Gamma(\gamma+3)} \, \hat{D}^{-\beta}\, {N_0}^{-\beta/4}\, (\rho\, q)^{\beta/4} \quad , \tag{21a}$$

$$\bar{w}_{t,00} = w_0 \quad \frac{\Gamma(\gamma+3+\beta)}{\Gamma(\gamma+3)} \, \left(\frac{D_0}{\hat{D}}\right)^{\beta} \quad . \tag{21b}$$

Note that Eq. (21b) is independent of $\rho\, q$.

In the general case in which an external vertical velocity field w is imposed so that with Eq. (2) the precipitation rate reads

$$R = -\bar{w}_s\, \rho\, q = -\left[w + \bar{w}_{t,00} \left(\frac{\rho_{00}}{\rho}\right)^{\alpha} \right] \rho\, q \quad . \tag{22}$$

Without loss of generality we may set

$$w = X\, \bar{w}_{t,00} \left(\frac{\rho_{00}}{\rho}\right)^{\alpha} \quad . \tag{23}$$

Here, negative values of X correspond to updrafts. The local value of w is a superposition of an imposed vertical wind and an additional downdraft component induced by the hydrometeor drag. Introducing Eq. (23) into Eq. (22) the expression for the rain rate becomes

$$R = -(X+1)\, \bar{w}_{t,00} \left(\frac{\rho_{00}}{\rho}\right)^{\alpha} \rho\, q \quad . \tag{24}$$

A.3 Z–R relations

As shown by Dotzek and Beheng (2001), the final Z–R relations take on the form

$$Z = a_{00,N}\, f_N(\rho)\, g_N(w)\, R^{7/(4+\beta)} \quad , \qquad \text{with} \quad f_N(\rho) = \left(\frac{\rho_{00}}{\rho}\right)^{-\alpha[7/(4+\beta)]} \quad , \tag{25a}$$

$$Z = a_{00,D}\, f_D(\rho)\, g_D(w)\, R \quad , \qquad \text{with} \quad f_D(\rho) = \left(\frac{\rho_{00}}{\rho}\right)^{-\alpha} \quad , \tag{25b}$$

in which the $f(\rho)$ present the density terms that can be corrected for. Dotzek et al. (2002) have used the term $f_N(\rho)$ in their radar data correction algorithm for $Z = a\, R^b$ and the fall speed law exponent α from Eq. (22):

$$Z_{\text{corr}} = Z \left(\frac{\rho_{00}}{\rho(z)}\right)^{\alpha\, b} \quad . \tag{26}$$

For precipitation aloft the measured radar reflectivity factor Z has to be increased according to this relation before any standard sea level Z–R relation can be applied to yield a representative rain rate R. That is both important for R profiles in high clouds and base level reflectivities of convective and stratiform clouds at large range. The latter was quantified by (Dotzek et al., 2002) in greater detail. For the case of KTLX WSR–88D radar in te USA, the authors showed that the precipitation accumulation from the corrected Z field can be 10 to 50 % higher for radar ranges from 100 to 300 km.

References

Adrian, G., and F. Fiedler, 1991: Simulation of unstationary wind and temperature fields over complex terrain and comparison with observations. *Contrib. Atmos. Phys.*, **64**, 27–48.

Aniol, R., J. Riedl, and M. Dieringer, 1980: Über kleinräumige und zeitliche Variationen der Niederschlagsintensität. *Meteor. Rundsch.*, **33**, 50–56.

Atlas, D., P. Willis, and F. Marks, 1995: The effects of convective up- and downdrafts on reflectivity–rain rate relations and water budgets. *Preprints, 27th Int. Conf. on Radar Meteor.*, Vail, Amer. Meteor. Soc., Boston, 19–22.

Atlas, D., C. W. Ulbrich, F. D. Marks Jr., E. Amitai, and C. R. Williams, 1999: Systematic variation of drop size and radar–rainfall relations. *J. Geophys. Res.*, **104**D, 6155–6169.

Austin, P. M., 1987: Relation between measured radar reflectivity and surface rainfall. *Mon. Wea. Rev.*, **115**, 1053–1070.

Battan, L. J., 1973: *Radar Observation of the Atmosphere*. Univ. Chicago Press, Chicago, 324 pp.

Battan, L. J., 1976: Vertical air motions and the Z–R relation. *J. Appl. Meteor.*, **15**, 1120–1121.

Beard, K. V., 1985: Simple altitude adjustments to raindrop velocities for Doppler radar analysis. *J. Atmos. Oceanic Tech.*, **2**, 468–471.

Dölling, I. G., J. Joss, and J. Riedl, 1998: Systematic variations of Z–R–relationships from drop size distributions measured in northern Germany during seven years. *Atmos. Res.*, **47–48**, 635–649.

Dotzek, N., 1998: Numerische Modellierung topographisch induzierter hochreichender konvektiver Wolken. *Ann. Meteor.*, **37**, 465–466.

Dotzek, N., 1999: *Mesoskalige numerische Simulation von Wolken- und Niederschlagsprozessen über strukturiertem Gelände*. Dissertation, Univ. Karlsruhe, 127 pp. [Available at www.op.dlr.de/˜pa4p/]

Dotzek, N., and K. D. Beheng, 2001: The influence of deep convective motions on the variability of Z–R relations. *Atmos. Res.*, **59–60**, 15–39. [Available at www.op.dlr.de/˜pa4p/]

Dotzek, N., J. J. Gourley, and T. Fehr, 2002: Vertical profiles of radar reflectivity and rain rate: Observational and modeling results. *ERAD Publ. Ser.*, **1**, 243–249. [Available at www.copernicus.org/erad/online/erad-243.pdf]

Douglas, R. H., 1964: Hail size distributions. *Preprints World Conf. on Radio Meteor. and Proc. 11th Radar Meteor. Conf.*, Boulder, 146–149.

Fehr, T., 2000: *Mesoskalige Modellierung der Produktion und des dreidimensionalen Transports von Stickoxiden in Gewittern*. Dissertation, Univ. Munich, 116 pp. [Available at www.op.dlr.de/˜pa10/]

Foote, G. B., and P. S. du Toit, 1969: Terminal velocity of raindrops aloft. *J. Appl. Meteor.*, **8**, 249–253.

Gourley, J. J., R. A. Maddox, K. W. Howard, and D. W. Burgess, 2002: An exploratory multisensor technique for quantitative estimation of stratiform rainfall. *J. Hydrometeor.*, **3**, 166–180.

Grell, G. A., J. Dudhia, and D. R. Stauffer, 1994: A description of the fifth–generation Penn State / NCAR mesoscale model (MM5). Tech. Rep. NCAR / TN–398 + STR, NCAR, Boulder, 122 pp.

Hannesen, R., N. Dotzek, H. Gysi, K. D. Beheng, 1998: Case study of a tornado in the Upper Rhine valley. *Meteor. Zeitschr.*, N. F., **7**, 163–170. [Available at www.op.dlr.de/˜pa4p/]

Jameson, A. R., and A. B. Kostinski, 2002: When is rain steady? *J. Appl. Meteor.*, **41**, 83–90.

Jordan, P., A. Seed, and G. Austin, 2000: Sampling errors in radar estimates of rainfall. *J. Geophys. Res.*, **105**D, 2247–2257.

Joss, J., and A. Waldvogel, 1990: Precipitation measurement and hydrology. Pp. 577–618. In: Atlas, D. (Ed.), *Radar in Meteorology*, Amer. Meteor. Soc., Boston, 806 pp.

Kessler, E., 1969: *On the distribution and continuity of water substance in atmospheric circulation*. Meteor. Monogr., **10**(32), Amer. Meteor. Soc., Boston, 84 pp.

Klemp, J. B., and R. B. Wilhelmson, 1978: The simulation of three–dimensional convective storm dynamics. *J. Atmos. Sci.*, **35**, 1070–1096.

Marshall, J. S., and W. McK. Palmer, 1948: The distribution of raindrops with size. *J. Meteor.*, **5**, 165–166.

Sauvageot, H., 1992: *Radar Meteorology*. Artech House, Boston, 366 pp.

Smith, P. L., 1984: Equivalent radar reflectivity factors for snow and ice particles. *J. Climate Appl. Meteor.*, **23**, 1258–1260.

Smith, P. L., C. G. Myers, and H. D. Orville, 1975: Radar reflectivity factor calculations in numerical cloud models using bulk parameterizations of precipitation. *J. Appl. Meteor.*, **14**, 1156–1165.

Tao, W.–K., and J. Simpson, 1993: The Goddard Cumulus Ensemble model, Part 1: Model description. *Terr. Atmos. Oceanic Sci.*, **4**, 35–72.

Tartaglione, N., A. Buzzi, and M. Fantini, 1996: Supercell simulations with simple ice parameterization. *Meteor. Atmos. Phys.*, **58**, 139–149.

Wacker, U., and A. Seifert, 2001: Evolution of rain water profiles resulting from pure sedimentation: Spectral vs. parameterized description. *Atmos. Res.*, **58**, 19–39.

Weisman, M. L., and J. B. Klemp, 1982: The dependence of numerically simulated convective storms on vertical wind shear and buoyancy. *Mon. Wea. Rev.*, **110**, 504–520.

Weisman, M. L., and J. B. Klemp, 1984: The structure and classification of numerically simulated convective storms in directionally varying wind shears. *Mon. Wea. Rev.*, **112**, 2479–2498.

Wilhelmson, R. B., and J. B. Klemp, 1981: A three–dimensional numerical simulation of splitting severe storms on 3 April 1964. *J. Atmos. Sci.*, **38**, 1581–1600.

Wilson, J. W., and E. A. Brandes, 1979: Radar measurement of rainfall — a summary. *Bull. Amer. Meteor. Soc.*, **60**, 1048–1058.

Zawadzki, I., 1984: Factors affecting the precision of radar measurements of rain. *Preprints, 22th Int. Conf. on Radar Meteor.*, Zurich, Amer. Meteor. Soc., Boston, 251–256.

Tables

Table 1: Vertical profiles of virtual potential temperature Θ_v and relative humidity RH up to 10 km AGL used for the KAMM simulation.

$\frac{z}{\text{km AGL}}$	$\frac{\Theta_v}{\text{K}}$	$\frac{\text{RH}}{\%}$
10.0	333.19	4.89
9.5	326.34	6.60
9.0	320.47	8.23
8.5	316.26	9.68
8.0	314.51	11.25
7.5	313.20	12.90
7.0	311.81	13.51
6.5	309.78	08.35
6.0	307.58	23.28
5.5	306.28	20.97
5.0	304.68	43.13
4.5	303.96	39.57
4.5	302.43	57.73
3.5	300.11	73.75
3.0	298.11	93.06
2.5	296.20	98.45
2.0	294.41	86.88
1.5	293.46	68.51
1.0	292.93	65.12
0.5	293.03	63.48
0.0	294.30	61.87

Table 2: Maximum total hydrometeor mixing ratios, highest values of up- and downdrafts, and storm strength S (Weisman and Klemp, 1984) for both KAMM and MM5 model simulations.

Stage	$\frac{t}{\text{LST}}$	$\frac{\rho\, q_{\text{tot,max}}}{\text{g m}^{-3}}$	$\frac{w_{\text{max}}}{\text{m s}^{-1}}$	$\frac{w_{\text{min}}}{\text{m s}^{-1}}$	S
KAMM					
(a)	1220	12.34	11.10	–1.97	0.37
(b)	1230	15.67	5.78	–5.10	0.19
(c)	1245	8.52	3.16	–9.75	0.11
MM5					
IC	1630	11.05	27.43	–12.27	0.53
SC	1730	10.18	37.73	–19.29	0.73
SC	1930	4.02	16.37	–11.38	0.32
MC	1730	8.90	28.33	–10.19	0.55
MC	1930	9.60	36.67	–20.49	0.71

Figure captions

Figure 1: Conceptual view of precipitation with and without mean wind $\bar{\boldsymbol{v}}(z)$ plus convection. For a rain cell with $R = 0$ at the ground, application of a Z–R relation implies accumulated precipitation P_{ac} right below the cloud (small graph a). In reality, hydrometeor trajectories at later times will lead to P_{ac} (subgraph b).

Figure 2: Projection of maximum reflectivities derived from the KAMM single cell storm simulation onto the x,z plane in different stages of cumulonimbus development: (a) 1220 LST growth, (b) 1230 LST maturity, and (c) 1245 LST decay. Light grey shading shows cloud dimensions ($Z \geq 0$ dBZ), regions with $Z \geq 40$ dBZ appear in dark grey.

Figure 3: Model initialization sounding used for the MM5 split storm simulation (Fehr, 2000).

Figure 4: Evolution of MM5 multicell / supercell system shown by the total hydrometeor concentration at 4.4 km AGL altitude. Location of the gust front is also shown, labels are minutes simulation time, starting at 1600 LST.

Figure 5: Scattergrams between rain rate $R(\boldsymbol{r}, z)$ and height z for rain, snow $(+)$ cloud ice $(*)$, and cloud water $(\circ)$ without (panels a–c) and with vertical convective motions (panels d–f) for KAMM. Crosses $(\times)$ denote total precipitation rate.

Figure 6: Horizontally averaged rain rate profiles for the KAMM single cell storm. Cloud growth (1220, solid), cloud maturity (1230, dashed), and cloud decay (1245, dotted). In panel (a), w is set to zero, while panel (b) covers the general case $w \neq 0$. For the latter, graph (c) gives $\langle R_c \rangle$ only, while (d) shows $\langle R_r + R_i \rangle$ only.

Figure 7: Scattergrams between rain rate $R(\boldsymbol{r}, z)$ and height z for rain and graupel ($+$), cloud ice and snow ($*$), and cloud water ($\circ$) without (a) and with vertical convective motions (b) at the MM5 initial cell stage $t = 30$ min. Crosses ($\times$) denote total precipitation rate.

Figure 8: As Fig. 7, but for the right–moving MM5 supercell storm at times $t = 90$ min (a, b) and $t = 210$ min (c, d).

Figure 9: Horizontally averaged rain rate profiles $\langle R \rangle(z)$ for the MM5 supercell. Cloud growth (30 min, solid), maturity (90 min, dashed), and decay (210 min, dotted). In panel (a), $w = 0$.

Figure 10: Same scattergrams of $R(\boldsymbol{r}, z)$ and z as in Fig. 8, but for the left–moving MM5 multicell storms.

Figure 11: Horizontally averaged R profiles as in Fig. 9, but for the left–moving MM5 multicell storms.

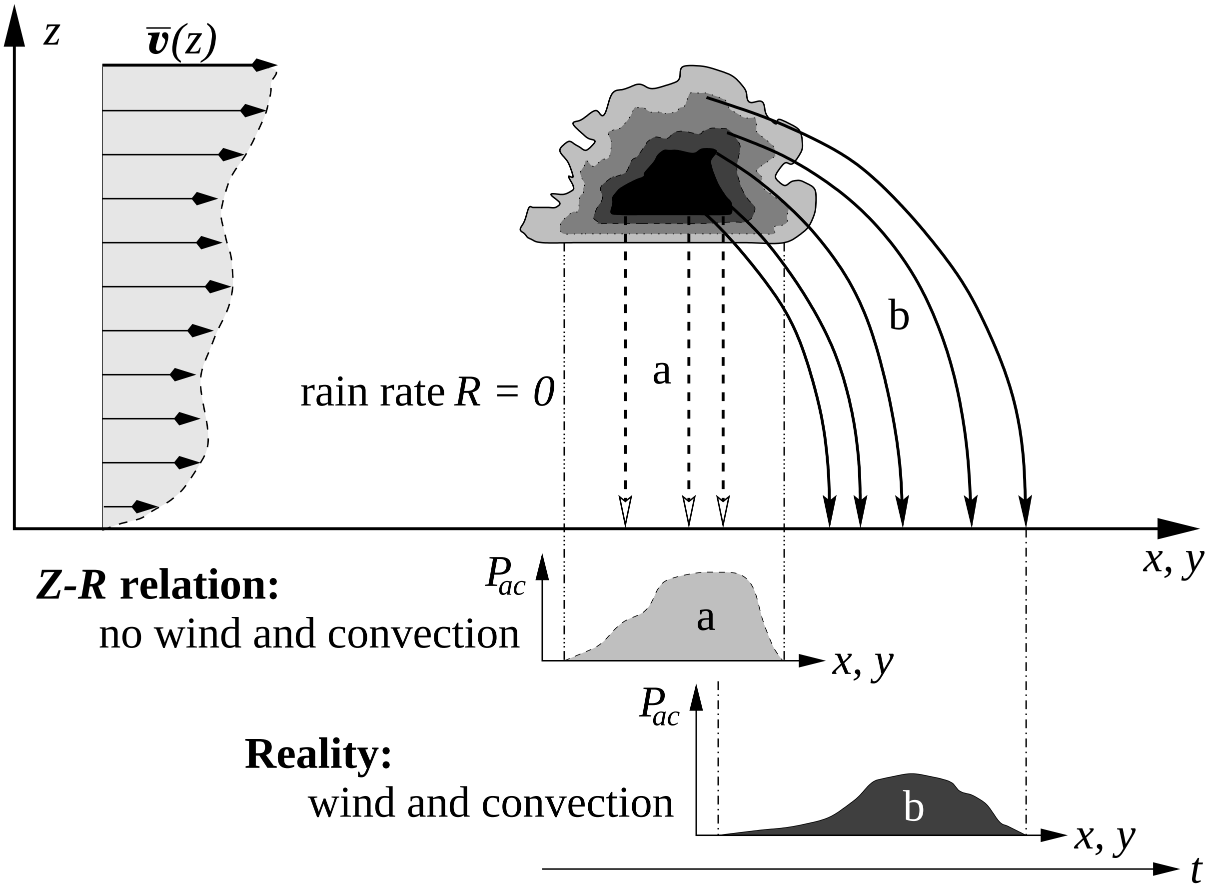
z
v̄(z)
rain rate R = 0
a
b
x, y
Z-R relation:
no wind and convection
Pac
a
x, y
Pac
Reality:
wind and convection
b
x, y
t

Figure 1

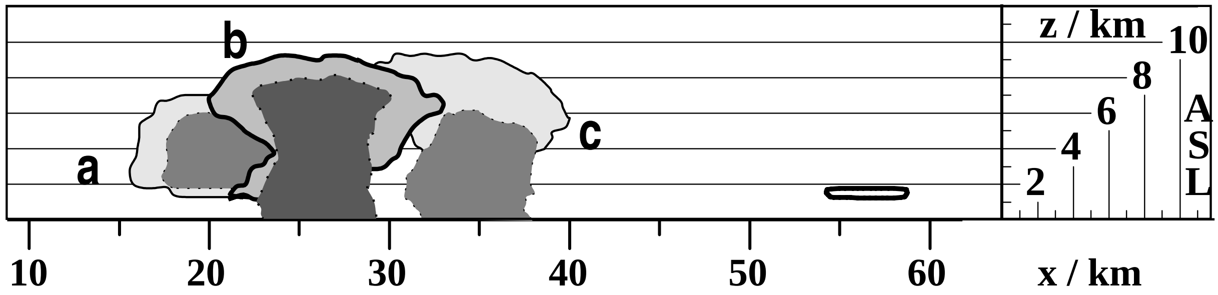

Figure 2

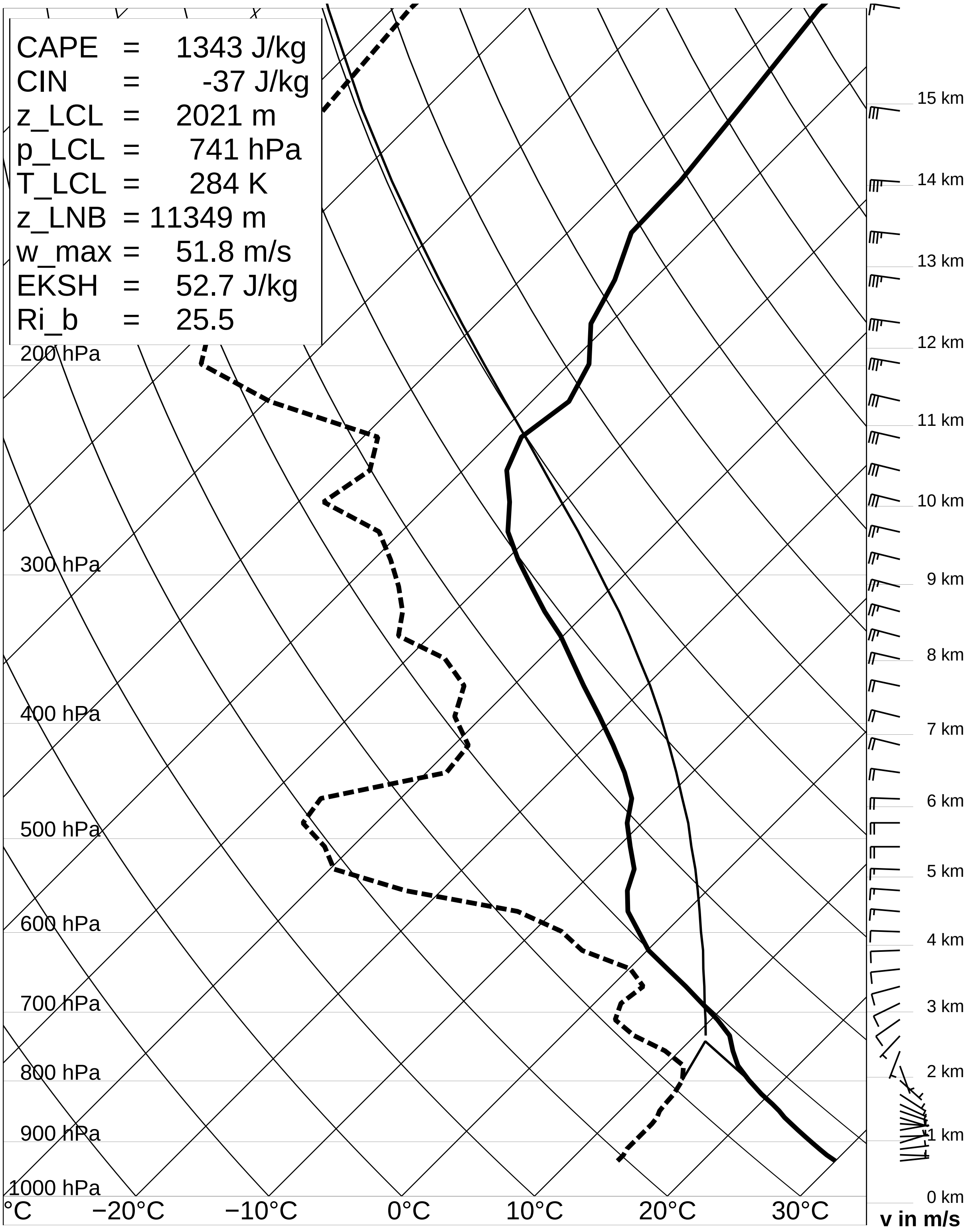
CAPE = 1343 J/kg
CIN = -37 J/kg
z_LCL = 2021 m
p_LCL = 741 hPa
T_LCL = 284 K
z_LNB = 11349 m
w_max = 51.8 m/s
EKSH = 52.7 J/kg
Ri_b = 25.5
200 hPa
300 hPa
400 hPa
500 hPa
600 hPa
700 hPa
800 hPa
900 hPa
1000 hPa
°C
−20°C
−10°C
0°C
10°C
20°C
30°C
15 km
14 km
13 km
12 km
11 km
10 km
9 km
8 km
7 km
6 km
5 km
4 km
3 km
2 km
1 km
0 km
v in m/s

Figure 3

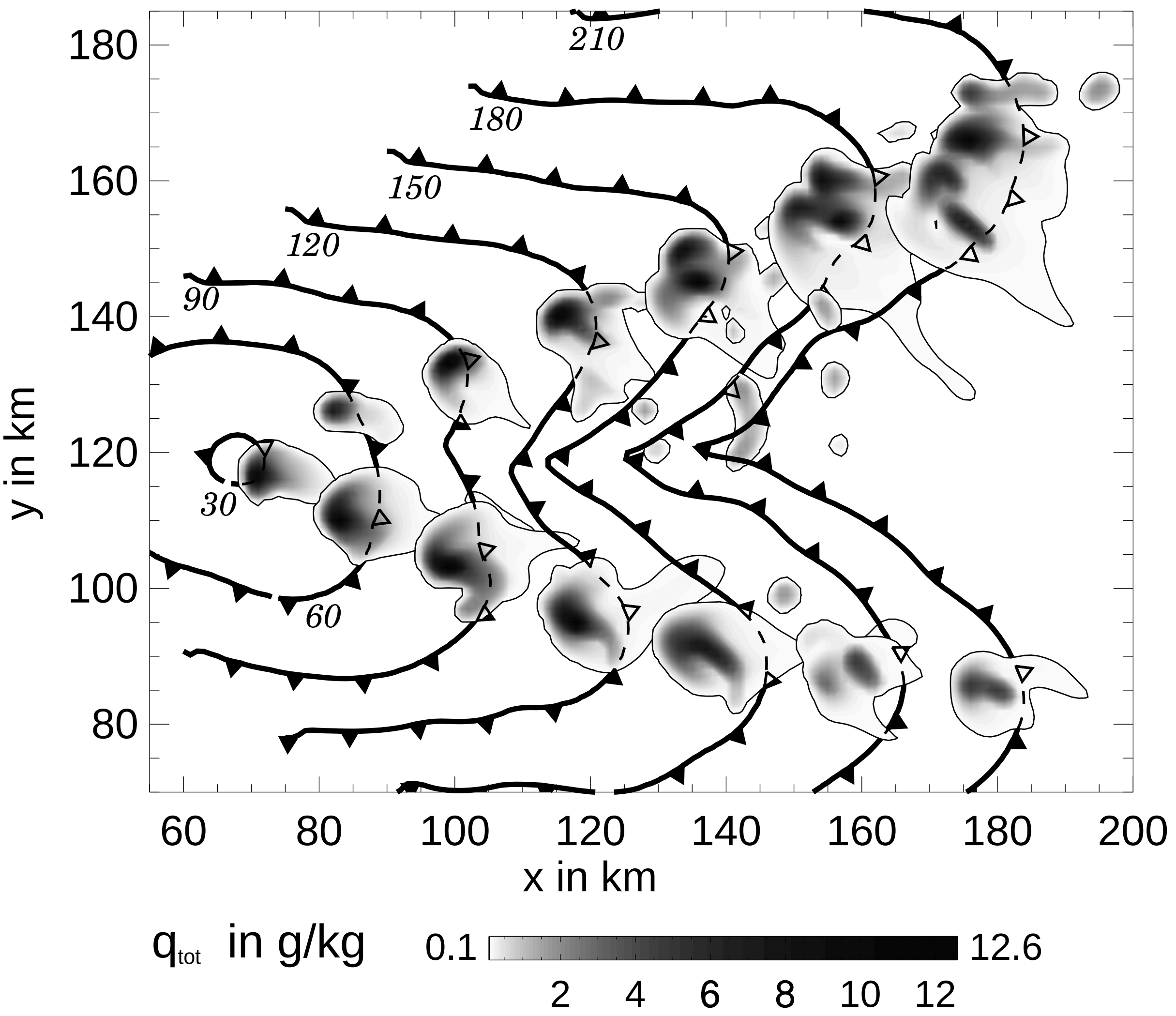

180
160
140
120
100
80
y in km
60
80
100
120
140
160
180
200
x in km
210
180
150
120
90
30
60
q$_{tot}$ in g/kg
0.1
12.6
2
4
6
8
10
12

Figure 4

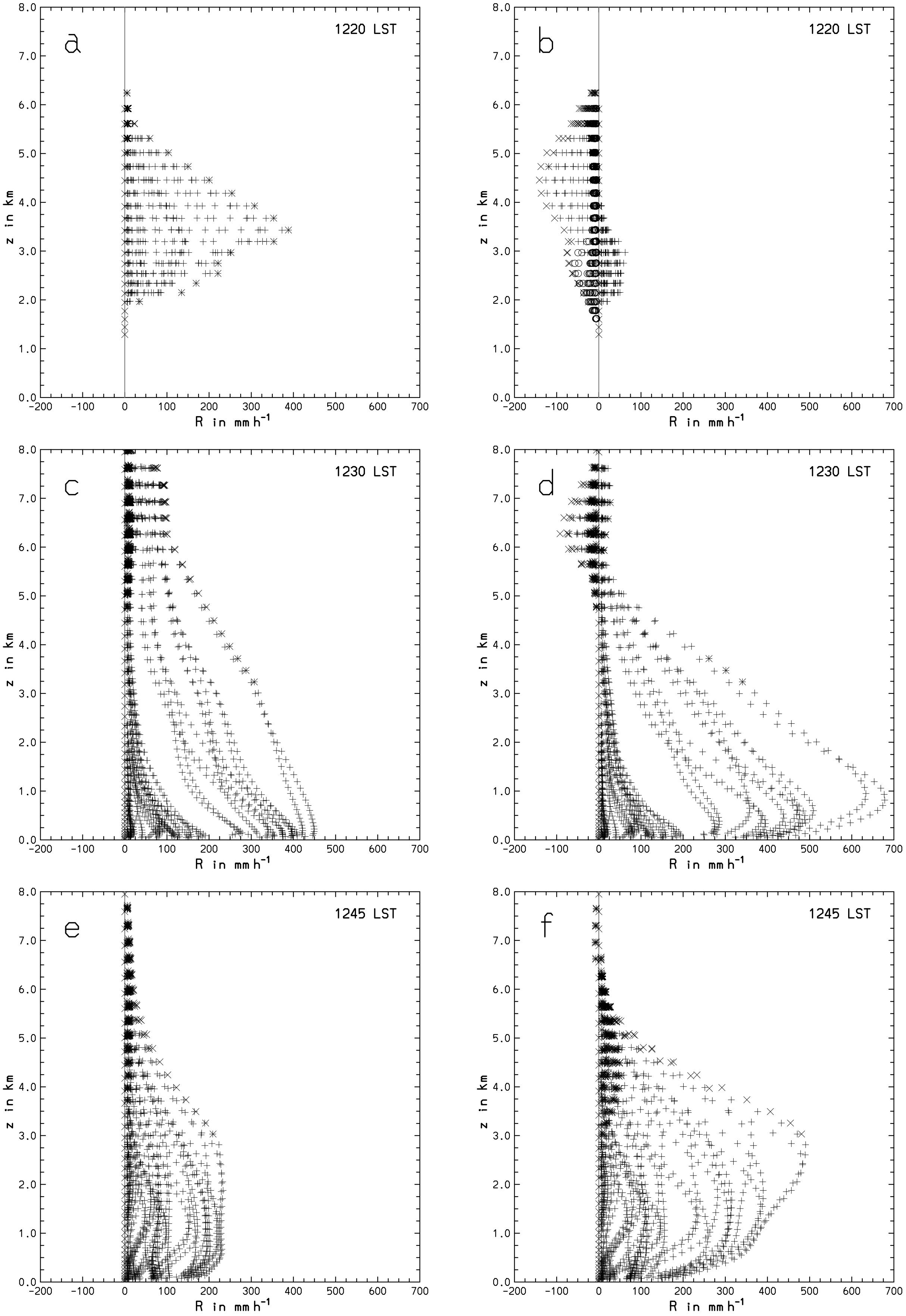

a
1220 LST
b
1220 LST
c
1230 LST
d
1230 LST
e
1245 LST
f
1245 LST
z in km
R in mm h^{-1}
0.0
1.0
2.0
3.0
4.0
5.0
6.0
7.0
8.0
−200
−100
0
100
200
300
400
500
600
700

Figure 5

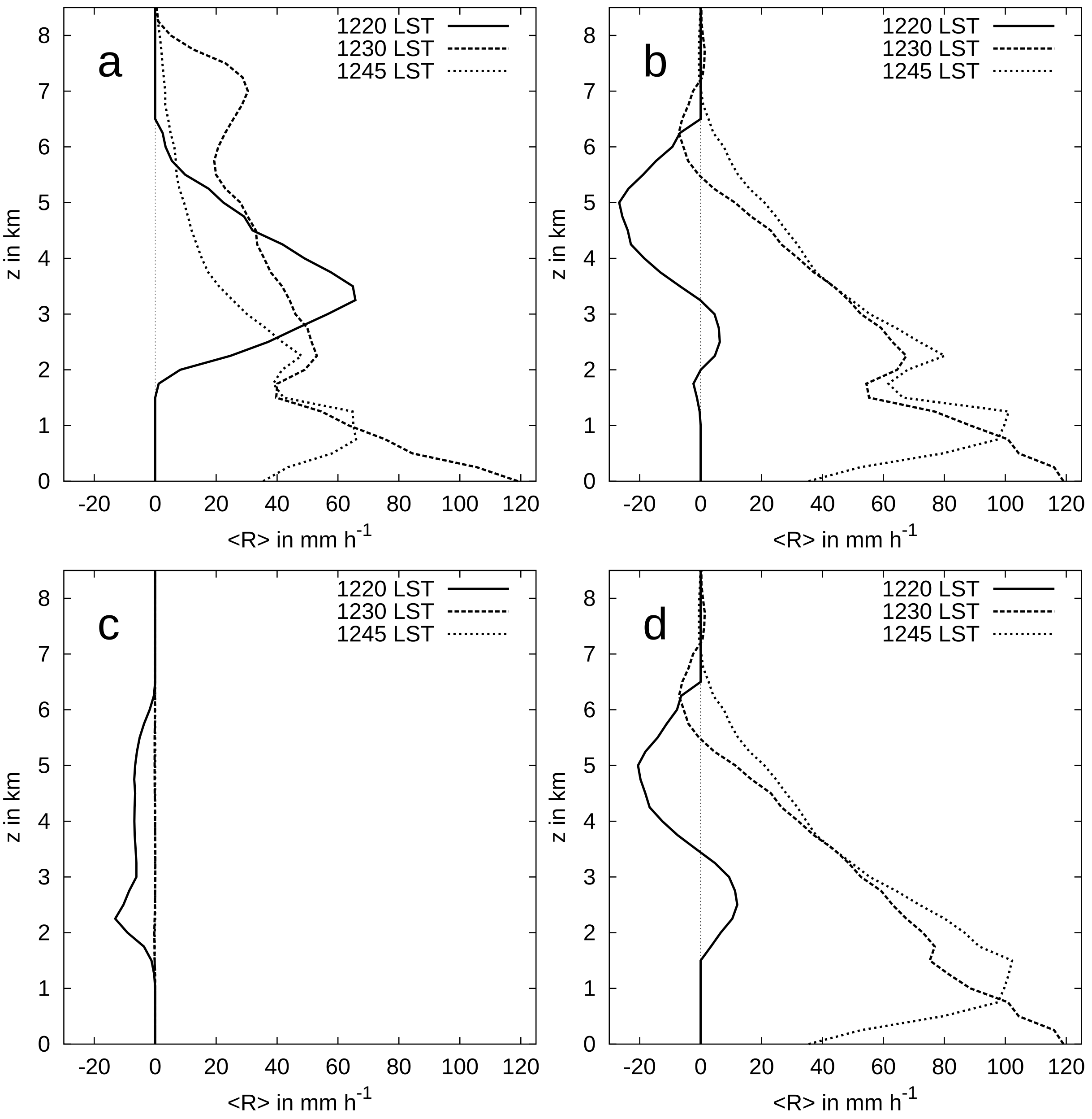
a
b
c
d
1220 LST
1230 LST
1245 LST
z in km
<R> in mm h^{-1}
0
1
2
3
4
5
6
7
8
-20
0
20
40
60
80
100
120

Figure 6

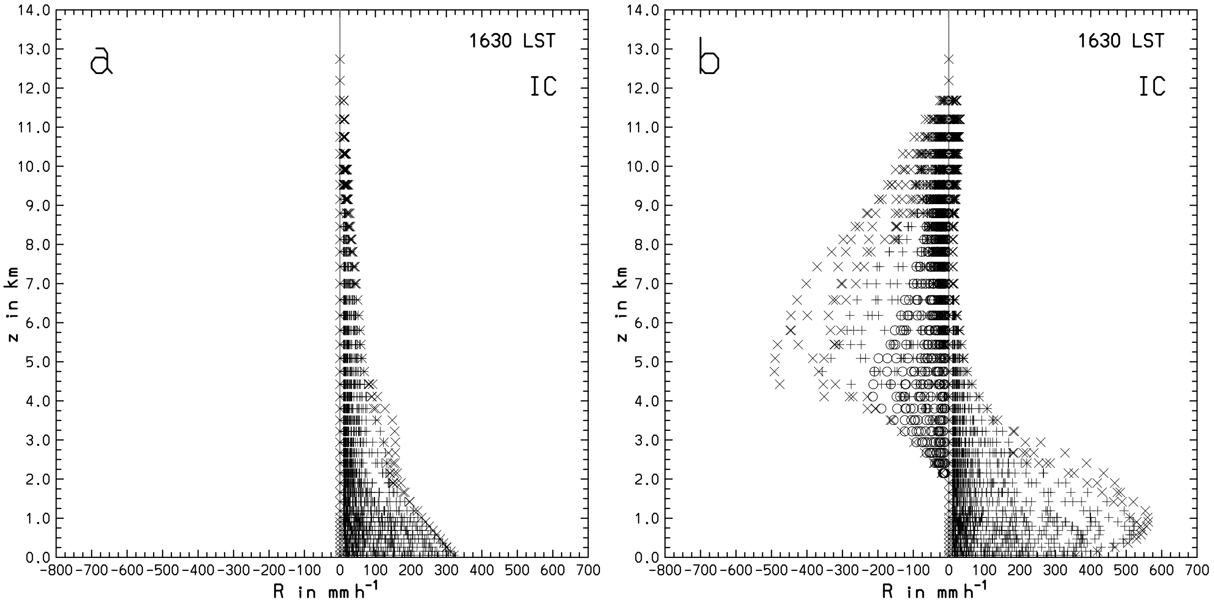
a
b
1630 LST
IC
z in km
R in mm h^{-1}
0.0
1.0
2.0
3.0
4.0
5.0
6.0
7.0
8.0
9.0
10.0
11.0
12.0
13.0
14.0
-800 -700 -600 -500 -400 -300 -200 -100 0 100 200 300 400 500 600 700

Figure 7

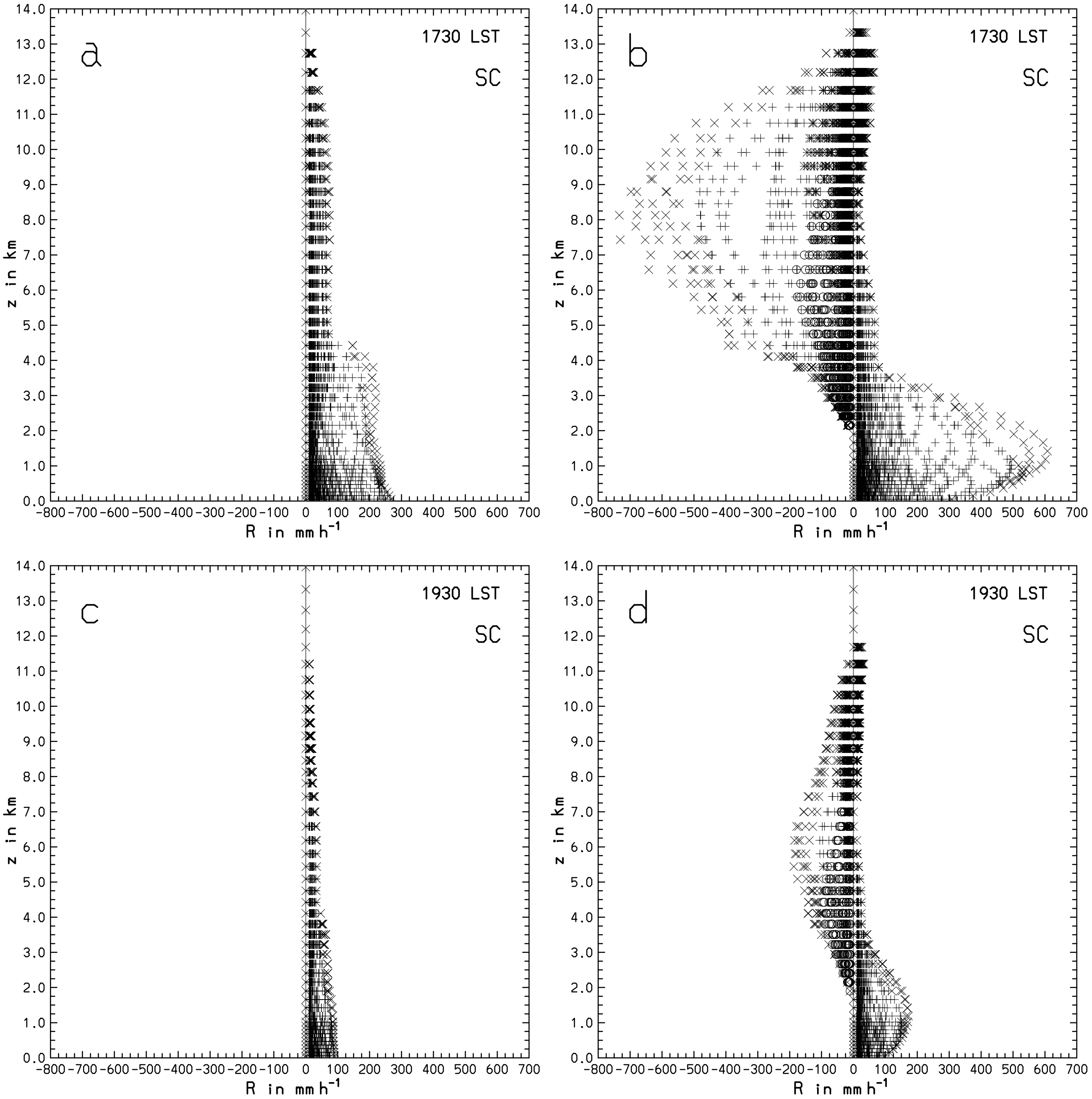
a
b
c
d
1730 LST
1930 LST
SC
z in km
R in mm h^{-1}
14.0
0.0
-800 -700 -600 -500 -400 -300 -200 -100 0 100 200 300 400 500 600 700

Figure 8

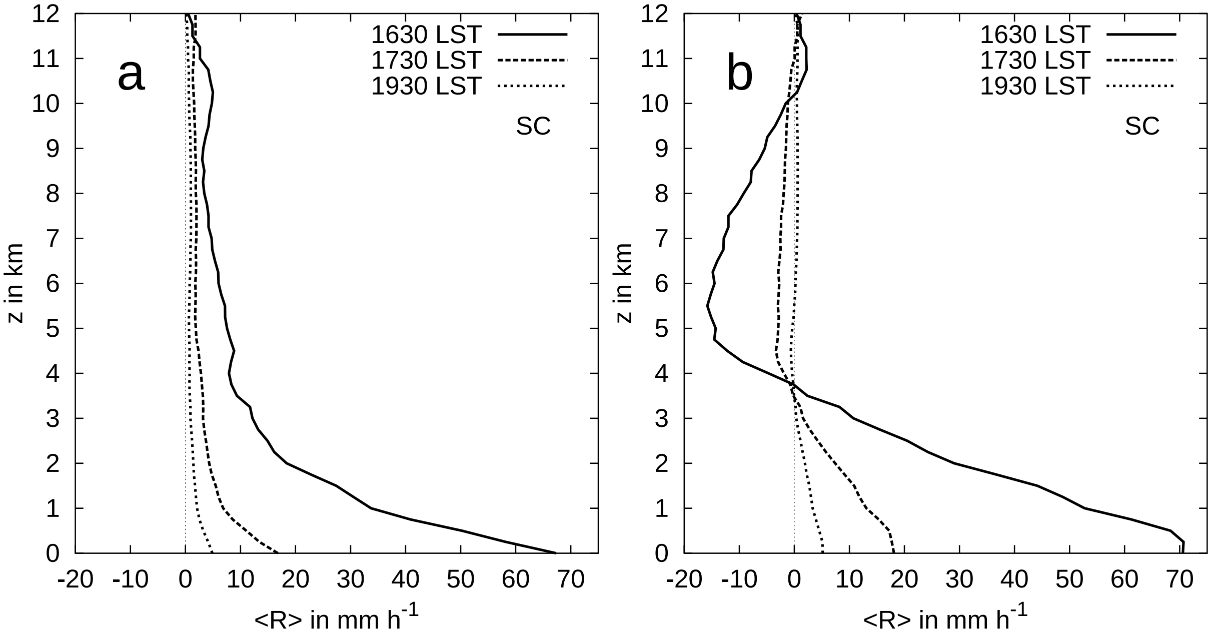
a
b
1630 LST
1730 LST
1930 LST
SC
z in km
<R> in mm h^{-1}
0
1
2
3
4
5
6
7
8
9
10
11
12
-20
-10
0
10
20
30
40
50
60
70

Figure 9

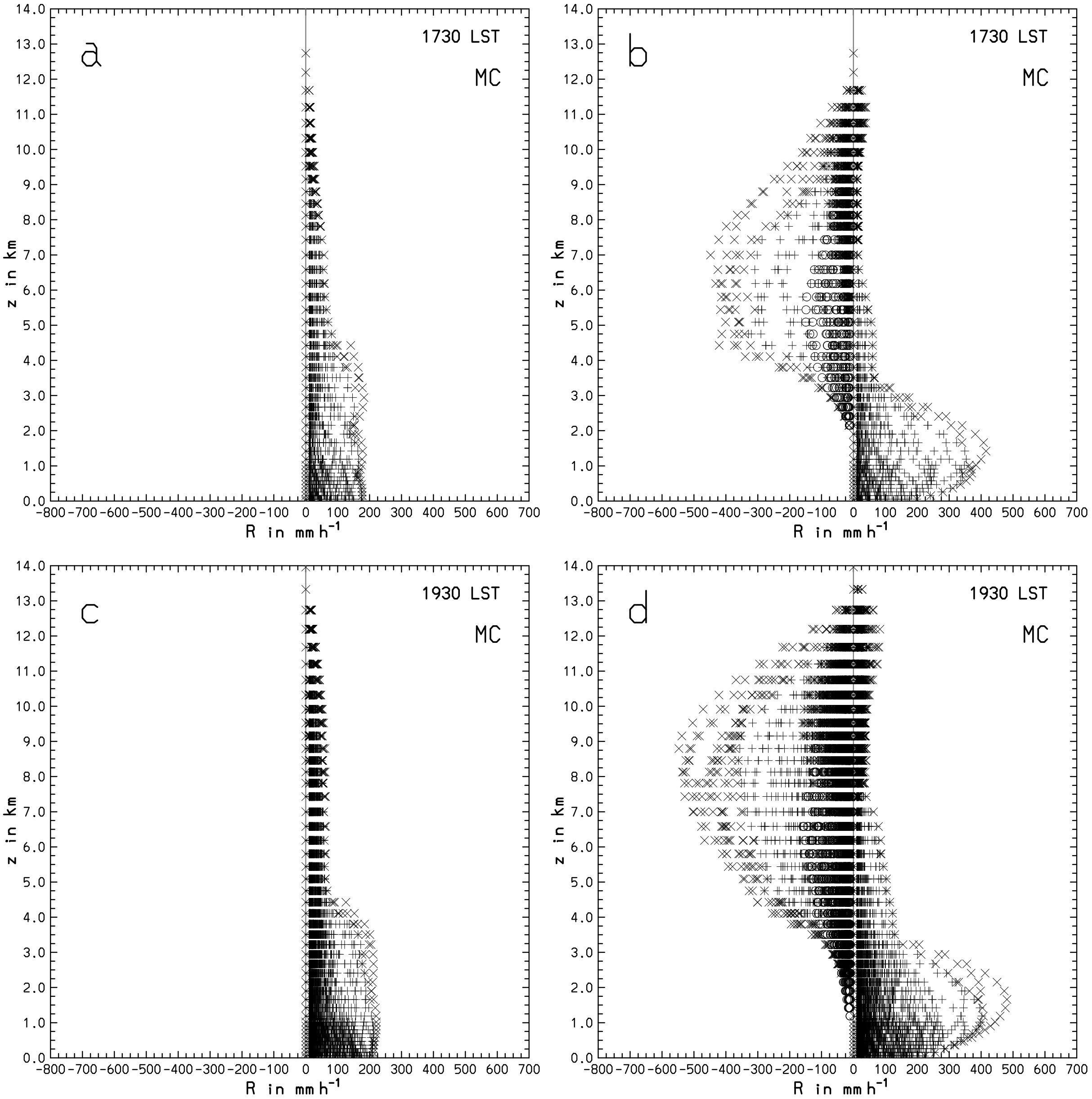
a
1730 LST
MC
b
1730 LST
MC
c
1930 LST
MC
d
1930 LST
MC
z in km
R in mm h^{-1}
0.0
1.0
2.0
3.0
4.0
5.0
6.0
7.0
8.0
9.0
10.0
11.0
12.0
13.0
14.0
−800 −700 −600 −500 −400 −300 −200 −100 0 100 200 300 400 500 600 700

Figure 10

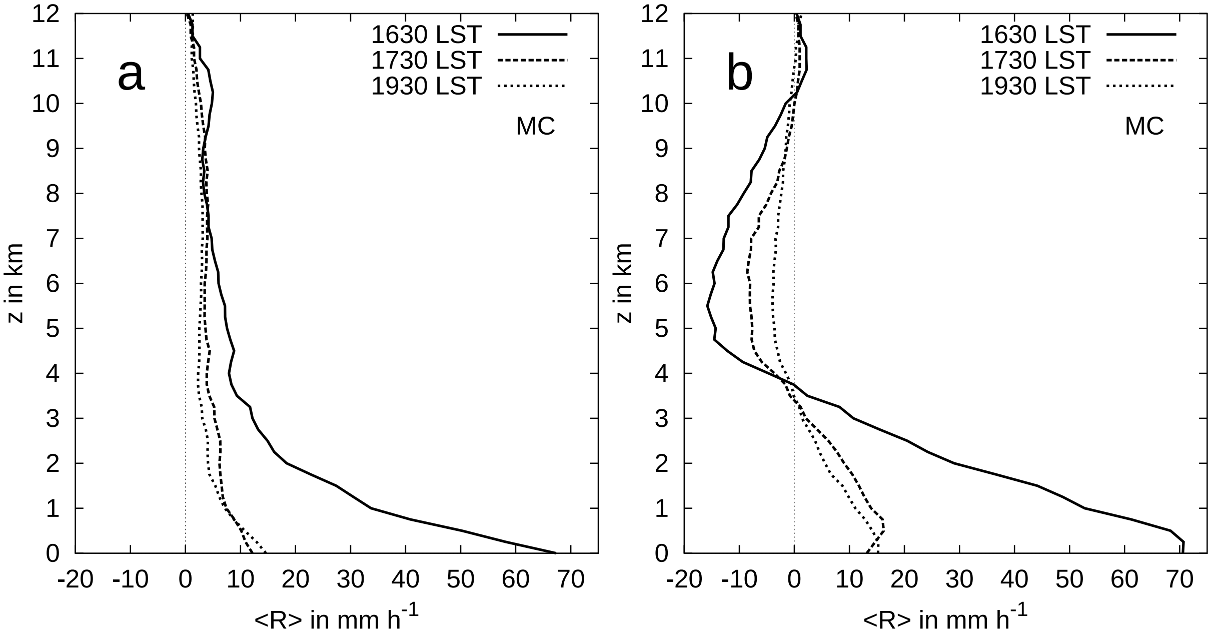
a
b
1630 LST
1730 LST
1930 LST
MC
z in km
<R> in mm h^{-1}
0
1
2
3
4
5
6
7
8
9
10
11
12
-20
-10
0
10
20
30
40
50
60
70

Figure 11